Flyback Micro-Converter Design with an Integrated Octagonal Micro-Transformer for DC-DC Conversion

Mokhtaria Derkaoui[1]* and Yamina Benhadda[2]

[1]*LARATIC laboratory, National Higher School of Telecommunications & ICT (ENSTTIC-Oran), Algeria; mokhtaria.derkaoui@ensttic.dz*
[2]*LEPA laboratory, University of Sciences and Technology of Oran (USTO- MB), Algeria; benhadda_yamina@yahoo.fr*

***Correspondence:** Mokhtaria Derkaoui; mokhtaria.derkaoui@ensttic.dz

ABSTRACT- The work presented in this paper concerns the design of an integrated flyback DC-DC micro-converter operating at high frequencies. The flyback converter consists of only one transformer. The integrated micro-transformer in the flyback micro-converter is composed of two planar stacked coils with spiral octagonal geometry. Basing on Mohan's method, the geometrical parameters are evaluated. The different parasitic effects created in the stacked layers are grouped perfectly in the equivalent electrical circuit that summarizes all parasitic effects. The integrated micro-transformer is characterized by scattering parameters extraction. The thermal and electromagnetic effects generated in the micro-transformer are illustrated, using finite elements method on COMSOL Multiphysics 5.3 software. To validate the electrical model, the simulation of the flyback micro-converter containing the equivalent electrical circuit of the micro-transformer is established, using PSIM 9.0 software. The gap between the coils is considered as an integrated MIM capacitor created at high frequencies leads to create a low pass micro-filter with the secondary coil.

Keywords: Flyback Micro-Converter; Integration; Micro-Filter; Micro-Transformer; Planar.

1. INTRODUCTION

The objective of the integration of passive components is to make the converter fully integrated and stand-alone. The majority of surface is occupied by discrete passive components. To overcome this problem, the integrated components were introduced [1-2]. Planar micro-transformers are currently extensively used in integrated circuits in many systems for several RF applications [3-4]. The integration allows to compact the small size components with better efficiency and low fabrication costs [5-6]. The easier technique for reducing sizes is to increase the operating frequency. Increasing the frequency has an impact for inductive components as the inductance, the size and the current. At high frequencies, inductive components can have a smaller size and hence smaller inductance [7-8]. Many researchers presented various studies that aim to integrate the micro-transformer in the micro-converter. [9-10] presented the design and modeling of an octagonal planar inductor and transformer for integration into a converter. They performed an electromagnetic and thermal simulation. [11-12] presented a numerical simulation study of the magneto-thermal behavior

allowing for an improved design of a square planar coil sandwiched between two magnetic materials. [13-14] presented a method of dimensioning a square spiral planar coil integrated in high voltage converter application a photovoltaic. They visualized the density of the magnetic flux and the electric potential. [15-16] developed a numerical model to determine the inductances of an elliptical planar transformer and its parasitic components. They demonstrated that the overall average error between the measured and proposed numerical model results was less than 5%.[17] presented a dimensioning and thermal modelling of a multilayer capacitor at low temperature cofired ceramic intended to be inserted in a low voltage converter.[18] performed a detailed study for designing an integrated structure with a dual-layer micro-transformer model associated with two layers of magnetic cores. Their research focused the impact of thickness of a planar coil on the inductance value.[19] numerically visualized by the finite element method the thermal behavior of an integrated transformer operating in a DC-DC micro converter. They determined the operating temperature in the different layers of the component in the transient and stationary state. The aim of our work is the design of a DC-DC micro-converter containing an octagonal planar spiral micro-transformer. The micro-converter is operating for low powers and high frequencies. The micro-transformer is composed of two stacked coils of three and two turns of primary and secondary respectively. The dimensioning of different geometric and electric parameters is required to integrate the micro-transformer in the micro-converter. The geometric parameters describe the sizes of the coils and the different layer added in the micro-transformer and the electric parameters describe the different parasitic effects generated in the different layers due to the high frequency. Using the finite elements method allows to show the thermal and

electromagnetic effects created in the micro-transformer operating at high frequencies. The addition of a ferrite magnetic material layer shows its importance in the micro-transformer. The simulations of the global integrated structure of DC-DC flyback micro-converter with the integrated micro-transformer validate the studies and the MIM capacitor allows to create an integrated low pass micro-filter.

2. FLYBACK MICRO-CONVERTER PRESENTATION

The converter is the main step of the design and dimensioning of passive components. We have opted for a flyback DC-DC converter *figure 1* for it contains just one transformer. The Flyback operation is based on the energy transfer from primary to secondary through a transformer [16].
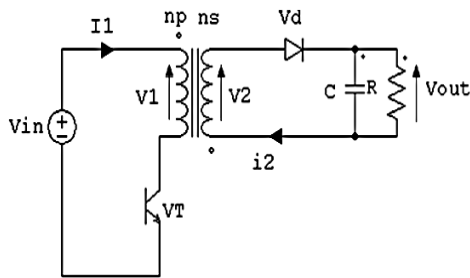

Figure 1: Electrical circuit of DC-DC flyback converter

Our target is to integrate completely the converter and to reduce its sizes. From the main parameters of the DC-DC flyback micro-converter (Input voltage Vin=12V, Output voltage V_{out} =5V, Duty cycle α=0.5, Output power P_{out}=5W, Operating frequency f =1GHz), we calculate the primary and secondary inductances (L_p, L_s) of the micro-transformer and their turn ratio m (*Equations 1-3*) [16].

$$L_p = \frac{V_{in}^2 \cdot \alpha^2}{2.f.P_{out}} \tag{1}$$

$$m = \frac{\alpha}{1-\alpha} \cdot \frac{V_{out}}{V_{in}} \tag{2}$$

$$L_s = m^2 . L_p \tag{3}$$

3. DIMESONING OF MICRO-TRANSFORMER

In this work, the integrated micro-transformer is composed of two stacked planar coils and their topologies are spiral octagonal *figure 2*.
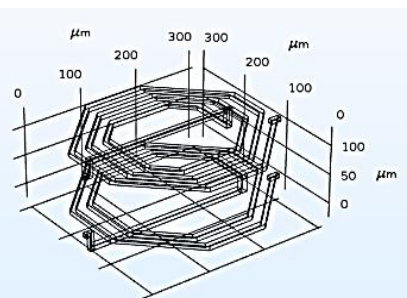

Figure 2: Octagonal spiral planar micro-transformer

The octagonal micro-transformer is defined by geometrical parameters. The outer diameter is equal to 500 µm, the angles are equivalent to multiples of 45 degrees.

Primary and secondary turn's number n_p, n_s
We find in literature several expressions that allow us to calculate the turn's number of micro-coils according to the inductance, we opted for Mohan's method [14] (*equations 4-5*).

$$n_p = \sqrt{\frac{2 \cdot L_p}{\mu_0 \cdot d_{avg} \cdot C_1 \cdot \left\{\ln\left(\frac{C_2}{\rho}\right) + C_3 \cdot \rho + C_4 \cdot \rho^2\right\}}} \tag{4}$$

$$n_s = \sqrt{\frac{2 \cdot L_s}{\mu_0 \cdot d_{avg} \cdot C_1 \cdot \left\{\ln\left(\frac{C_2}{\rho}\right) + C_3 \cdot \rho + C_4 \cdot \rho^2\right\}}} \tag{5}$$

$$d_{avg} = \frac{d_{out} + d_{in}}{2} \tag{6}$$

$$A_m = \frac{d_{out} - d_{in}}{d_{out} + d_{in}} \tag{7}$$

The coefficients C1, C2, C3 and C4 are defined for our octagonal geometry as C1= 1.07, C2= 2.29, C3=0, C4= 0.19. davg is the average diameter and ρ is the form factor [14].

Primary and secondary total length l_{tp}, l_{ts}
$$l_{tp} = n_p \cdot d_{avg} \cdot N \cdot \tan\frac{\pi}{N} \tag{8}$$

$$l_{ts} = n_s \cdot d_{avg} \cdot N \cdot \tan\frac{\pi}{N} \tag{9}$$

N is the number of sides which is 8 in our case.

Primary and secondary spacing sp, ss and width wp, ws are related to the inner and the outer diameter (Equations 10-11);

$$2 \cdot n_p \cdot w_p + 2 \cdot (n_p - 1) \cdot s_p = d_{out} - d_{in} \tag{10}$$

$$2 \cdot n_s \cdot w_s + 2 \cdot (n_s - 1) \cdot s_s = d_{out} - d_{in} \tag{11}$$

4. MODELING OF INTEGRATED MICRO-TRANSFORMER

Our integrated micro-transformer model is composed of two octagonal spiral planar coils in copper stacked on dielectric layer of silicon nitride Si3N4, magnetic layer of ferrite NiFe and substrate layer of silicon Si *figure 3a*.
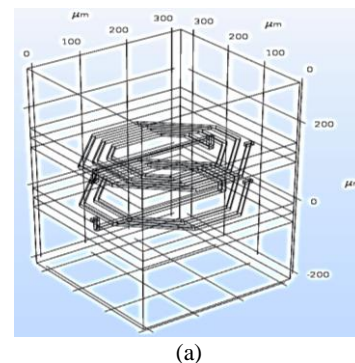
(a)

When the micro-transformer operates at 1 GHz of frequency, the coupling capacitances are created in parallel with inductances and in different layers. The equivalent electrical circuit of the micro-transformer displays the different parasitic effects created in the different layers at high frequencies *figure 3b*.
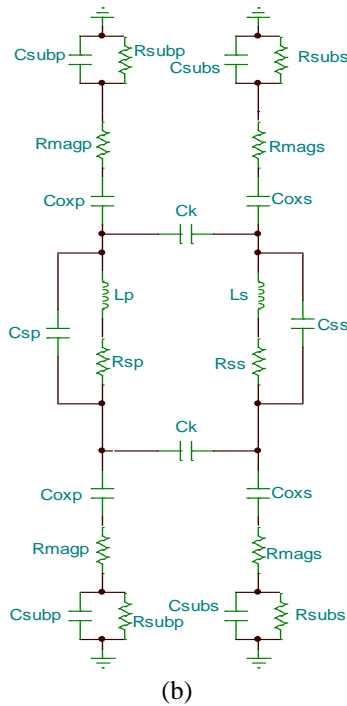

(b)

Figure 3: (a) Integrated micro-transformer model, (b) Equivalent electrical circuit [4][14]

The magnetic core volume (Equation 12) is related to the total magnetic stored energy Wt (Equation 13) and the maximum energy volume density Wvmax (Equation 14). Therefore, 0.050 mm3 of ferrite NiFe is necessary to store 1.2 nJ of energy.

$$V = \frac{W}{W_{vmax}} = 5.025 \ 10^{-11} m^3 \qquad (12)$$

$$W_t = \frac{1}{2} \cdot L_s \cdot i_{out}^2 = 1.2 \ 10^{-9} J \qquad (13)$$

$$W_{vmax} = \frac{B_{max}^2}{2 \cdot \mu_{NiFe}} = 23.88 \ J/m^3 \qquad (14)$$

Maximal saturation induction Bmax= 0.3 T

The electrical parameters of the equivalent electrical circuit are calculated as follows [16-18];

Primary and secondary magnetic resistance R_{magp}, R_{mags}

$$R_{magp} = 2 \cdot \rho_{NiFe} \cdot \frac{e_{NiFe}}{w_p.l_{tp}} \qquad R_{mags} = 2 \cdot \rho_{NiFe} \cdot \frac{e_{NiFe}}{w_s.l_{ts}} \qquad (15)$$

Ferrite resistivity ρNiFe= 103 Ω.m

Primary and secondary substrate resistance R_{subp}, R_{subs}

$$R_{subp} = 2 \cdot \rho_{Si} \cdot \frac{e_{Si}}{w_p \cdot l_{tp}} \qquad R_{subs} = 2 \cdot \rho_{Si} \cdot \frac{e_{Si}}{w_s \cdot l_{ts}} \qquad (16)$$

Silicon resistivity ρSi= 18.5 Ω.m

Primary and secondary oxide capacitance C_{oxp}, C_{oxs}

$$C_{oxp} = \frac{1}{2} \cdot \varepsilon_{Si_3N_4} \cdot \frac{w_p \cdot l_{tp}}{t_{gap}} \qquad C_{oxp} = \frac{1}{2} \cdot \varepsilon_{Si_3N_4} \cdot \frac{w_s \cdot l_{ts}}{t_{gap}} \qquad (17)$$

tgap is the spacing between primary and secondary coils, relative permittivity of Si3N4 equals to 6.

Primary and secondary substrate capacitance C_{subp}, C_{subs}

$$C_{subp} = \frac{1}{2} \cdot \varepsilon_{Si} \cdot \frac{w_p \cdot l_{tp}}{e_{si}} \qquad C_{subs} = \frac{1}{2} \cdot \varepsilon_{Si} \cdot \frac{w_s \cdot l_{ts}}{e_{si}} \qquad (18)$$

Relative permittivity of silicon is 11.8

Primary and secondary spacing capacitance C_{sp}, C_{ss}

$$Cs_p = \varepsilon_{Si3N4} \cdot \left| \frac{t}{\delta} + 0.15 \frac{t}{\delta} + 2.8 \left(\frac{s_p}{\delta} \right)^{0.222} \right| \cdot l_{tp}$$

$$Cs_s = \varepsilon_{Si3N4} \cdot \left| \frac{t}{\delta} + 0.15 \frac{t}{\delta} + 2.8 \left(\frac{s_s}{\delta} \right)^{0.222} \right| \cdot l_{ts} \qquad (19)$$

Primary and secondary coupling capacitance CK_p, CK_s

$$C_{kp} = \varepsilon_{Si3N4} \cdot \left| \frac{w_p}{\delta} + 0.15 \frac{w_p}{\delta} + 2.8 \left(\frac{t_{gap}}{\delta} \right)^{0.222} \right| \cdot l_{tp} \qquad C_{ks} =$$

$$\varepsilon_{Si3N4} \cdot \left| \frac{w_s}{\delta} + 0.15 \frac{w_s}{\delta} + 2.8 \left(\frac{t_{gap}}{\delta} \right)^{0.222} \right| \cdot l_{ts} \qquad (20)$$

Primary and secondary serial resistance Rsp, Rss

$$Rs_p = \rho_{cu} \cdot \frac{l_{tp}}{w_p \cdot t_{eff}} \qquad Rs_s = \rho_{cu} \cdot \frac{l_{ts}}{w_s \cdot t_{eff}} \qquad (21)$$

Copper resistivity ρCu = 1.7 10−8 Ω·m and teff is the effective thickness (*Equation 22*) [19],

$$t_{eff} = \delta \cdot \left(1 - e^{-(t/\delta)} \right) \qquad (22)$$

δ is the skin thickness (Equation 23), it depends on the frequency *figure 4* [19].

$$\delta = \sqrt{\frac{\rho_{Cu}}{\pi \cdot \mu_0 \cdot \mu_{rCu} \cdot f}} \qquad (23)$$
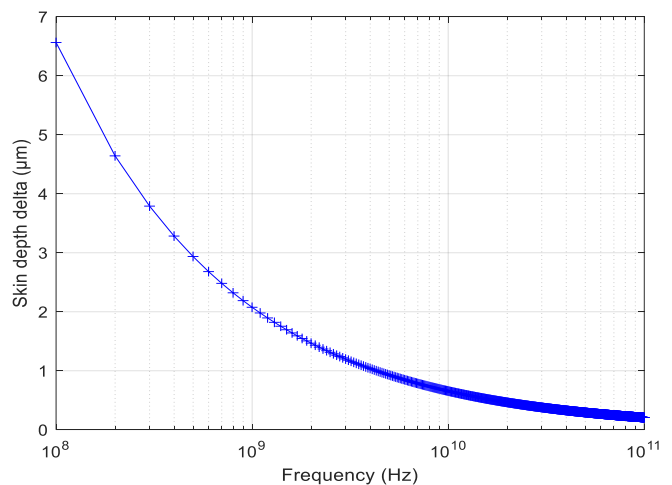

Figure 4: Skin thickness versus frequency

5. INTEGRATED MICRO TRANSFORMER CHARACTERIZATION

Scattering parameters characterize the electrical behaviour of the integrated planar micro-transformer. From the electrical model *figure 3b*, we obtain the S-parameters' matrix and also the Z-parameters [12][20]. S11 and S22 represent the reflection coefficients of the primary and secondary coils of micro-transformer. They are directly related to the impedance. S12 and S21 represent the transmission coefficients, they are commonly called gain or attenuation. The simulation was performed in the range of frequency between 100 MHz and 10 GHz.
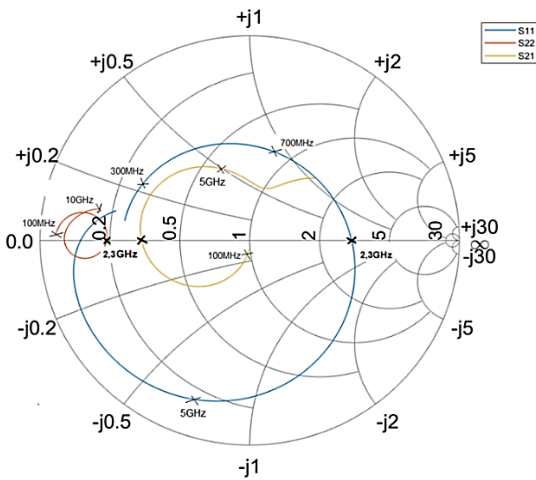
Figure 5: Scattering parameters S11, S22 and S21 of on-chip micro-transformer

As shown in *figure 5*, the S-parameters are represented in Smith chart. The curves of S11 and S22 display an inductance characterization. S11 shows a nearly short circuit at low frequencies (100 MHz). Therefore, S22 shows a very low impedance over the whole frequency range. The micro-transformer has a self-resonance frequency of about 2.3 GHz. The coupling factor k, given by Equation (24) [21], is shown on *figure 6* versus frequency. A k-factor of the micro-transformer is equal to 0.9 at the operating frequency 1 GHz.

$$k = \sqrt{\frac{\text{Imag}(Z_{12}).\text{Imag}(Z_{21})}{\text{Imag}(Z_{11}).\text{Imag}(Z_{22})}} \tag{24}$$
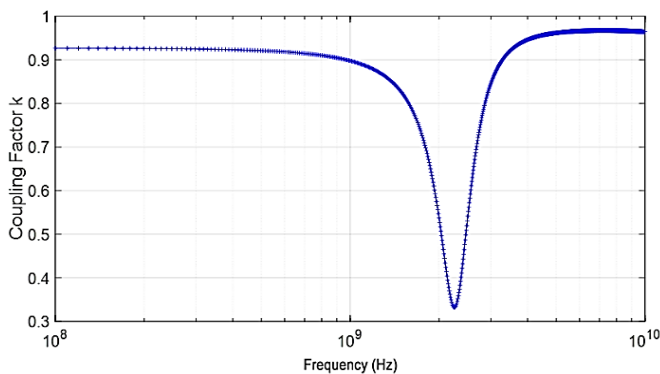

Figure 6: Coupling factor k versus frequency

The quality factor expresses losses in the micro-transformer, it is analysed using (Equations 25) [22-23],

$$Q_p = \frac{\text{Im}(Z_{11})}{\text{Re}(Z_{11})} \qquad Q_s = \frac{\text{Im}(Z_{22})}{\text{Re}(Z_{22})} \tag{25}$$
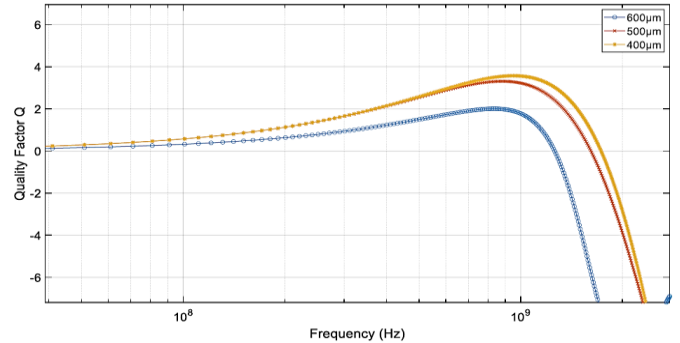

Figure 7: Quality factor versus frequency with different outer diameters

Figure 7 illustrates the measurement results with different outer diameters. We observe that the quality factor increases when the outer diameter decreases. The maximum values of the quality factors remain unchanged before the partial operating frequency. Thus, the Q factor is superior for the smaller micro-transformer when the frequency increases.
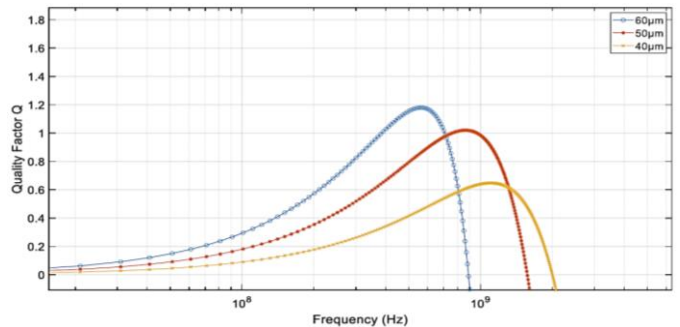

Figure 8: Quality factor over frequency with different width traces

Figure 8 illustrates the measurement results with different width. We observe that the Q factor is smaller when the traces are thinner. For lower frequencies the 60μm wide micro-transformer has a better Q-factor and the resonance frequency is close to the operating frequency, however the quality factor of the 40μm wide micro-transformer presents an important resonance frequency. The increase of the Q-factor for thin width traces is compensated by a reduction on the equivalent capacitance, which is related to the surface occupied by the micro-transformer.

6. THERMAL EFFECT IN THE INTEGRATED MICRO-TRANSFORMER

In this section, we show 3D simulations of thermal effects on the integrated micro-transformer.

6.1 Mathematical Model

The mathematical formulation (*Equation 26*) of the integrated micro-transformer is given by Green's function of heat conduction problems with heat source [24-25].

$$\frac{\partial^2 T}{\partial y^2} + \frac{1}{k} \cdot q = \frac{1}{\alpha} \cdot \frac{\partial T}{\partial t} \qquad (26)$$

To resolve *equation (26)*, we determine the analytical solution for homogeneous problem Th(y,t) and steady-state problem Ts(y), as *equation (27)*.

$$T(y,t) = Th(y,t) + Ts(y) \qquad (27)$$

The continuity conditions at the interfaces are given by (28);

$$\lambda_i \cdot \frac{dT}{dy} = \lambda_{i+1} \cdot \frac{dT_{i+1}}{dy} \qquad (28)$$

By resolving the heat equation (29) and taking into account certain boundary conditions, we determine the different thermal effects.

$$\rho \cdot C_p \cdot \frac{\partial T}{\partial t} - \nabla(k\nabla T) = q \qquad (29)$$

q: Heat source, ρ: Density [kg/m3], Cp: Heat capacity [J/K.kg], T: Calculated temperature [K], k: Thermal conductivity [W/m.K].

The convective heat transfer coefficient on faces is equal to 10 W/m².K representing the natural convection, the ambient absolute pressure equals to 105 Pa, the maximum weighted average temperature is 35°C, the ambient temperature is equal to 20°C, the accumulated power is 0.8 W, the power source equals to 0.79 W in the coils, the thermal diffusivity is equal to 0.85 10-4 m²/s *figure 9a*, the effective volume heat capacity is equal to 2 106 J/m3.K *figure 9b*, the heat capacity at constant pressure is 0.7 103 J/kg.K *figure 9c*, the average effective thermal conductivity equals to 250 W/m.K *figure 9d*.
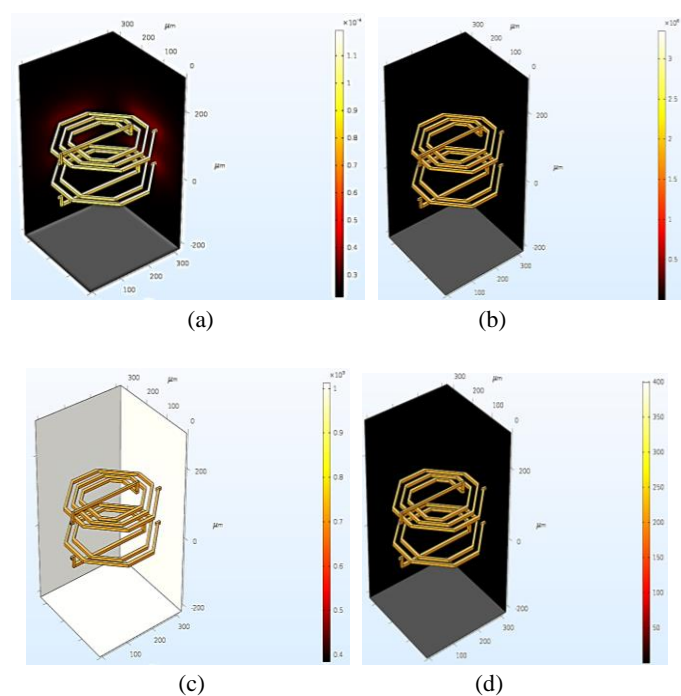

Figure 9: (a) Thermal diffusivity, (b) Effective volume heat capacity, (c) Heat capacity at constant pressure, (d) Average effective thermal conductivity, in the spiral coils

6.2 Visualization of the Thermal Behavior

Using Comsol Multiphysics 5.3 software and basing on finite elements method, we present the thermal effects in the micro-transformer. For a good precision, we choose the extremely fine mesh.
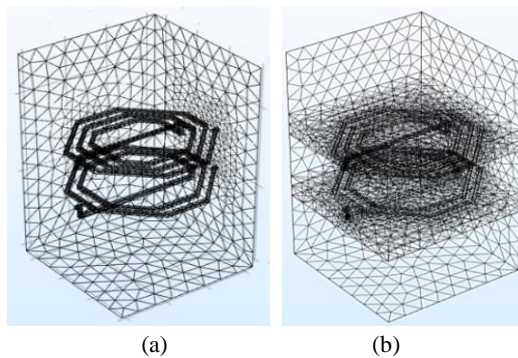

Figure 10: Mesh of the micro-transformer: (a) In air, (b) With different layers

Figure 10 shows the 3D extremely fine mesh of the integrated micro-transformer in the air and with all different layers.
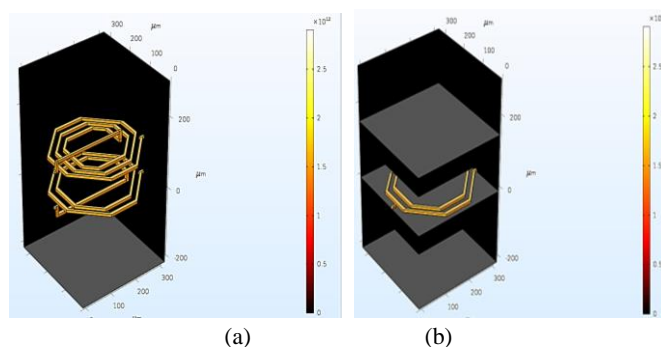

Figure 11: Total heat source in the micro-transformer: (a) In air, (b) With all layers

In *figure 11a*, we observe that the total heat source comes from the conductive coils of copper and it achieves 1.8 1012 W/m², whereas the other stacked layers don't contribute as the heat source.
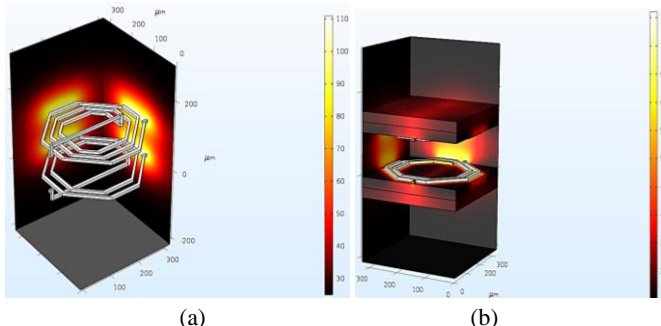

Figure 12: Temperature distribution in the micro-transformer: (a) In air, (b) With all layers

In *figure 12a*, we observe the distributed temperature in the micro-transformer alone in the air without the other layers. We observe that the temperature value achieves 110°C in the conductor coils in copper. *Figure 12b* shows the distributed

temperature in the micro-transformer composed of all different layers. We observe that the temperature values decrease to 75°C. Thus, adding the NiFe ferrite, which has a high permeability, for magnetic layer allows to reduce the temperature caused by Joule effect created by the current circulation in the conductor coils. We have compared our results with those from the literature [18][24] and we notice that they are the same.
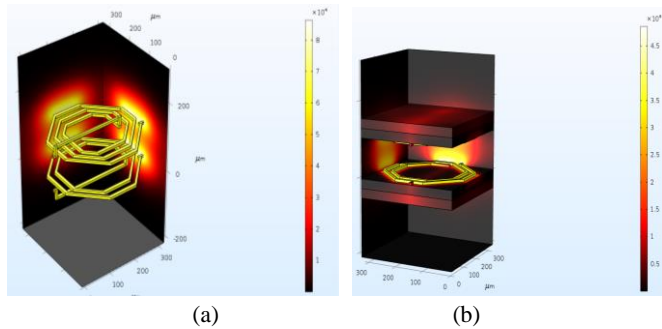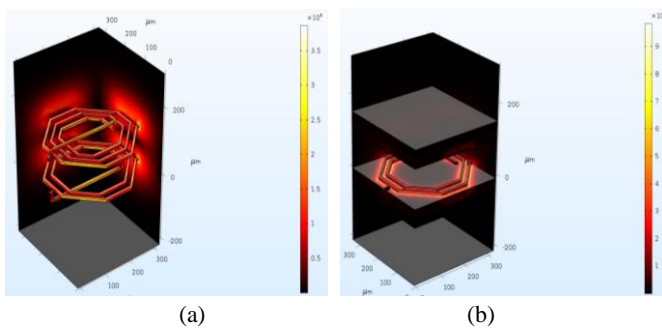

Figure 13: Enthalpy in the micro-transformer: (a) In air, (b) With all layers

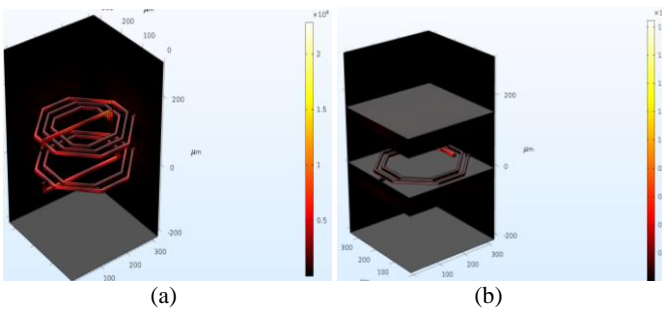**Figure 14:** Temperature gradient in the micro-transformer: (a) In air, (b) With all layers

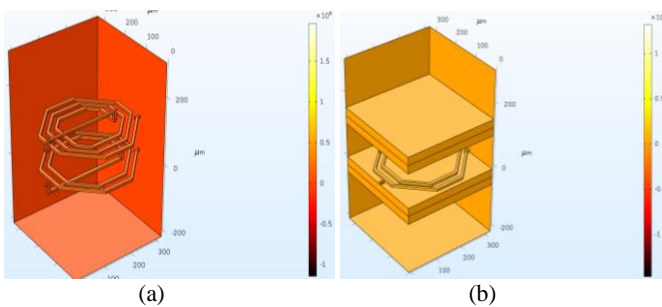**Figure 15:** Total heat flow in the micro-transformer: (a) In air, (b) With all layers

Figure 16: Heat flow by conduction in the micro-transformer: (a) In air, (b) With all layers

In *figure 13*, the enthalpy decreases to 4.5 10^4 J/Kg in the coils and it remains confined in the stacked micro-transformer. In *figure 14*, we observe that the temperature gradient increases and achieves 4 10^6 K/m in the coils. In *figure 15*, we observe that the total heat flow achieves 0.5 10^6 W/m² in the coils and it increases to 0.2 10^8 W/m² for the entire micro-transformer. In *figure 16*, we observe that the heat flow by conduction achieves 0.25 10^6 W/m² in the coils and it increases to 0.3 10^8 W/m² for the entire micro-transformer.

7. ELECTROMAGNETIC EFFECT IN THE INTEGRATED MICRO-TRANSFORMER

In this section, we show 3D simulations of electromagnetic effect on the integrated micro-transformer.

7.1 Mathematical Model

The electromagnetic effects are obtained by resolving Maxwell's electromagnetism equations [22-25] which link the electrical effect to the magnetic effect. The electrical effect is characterized by the displacement field D, the electric field E, the current density J and the density of free electric charges ρ_e. The magnetic effect is characterized by both the magnetic induction B and the magnetic field H (Equations 30 to 33).

$$\nabla \times \vec{E} = -\frac{\partial \vec{B}}{\partial t} \tag{30}$$

$$\nabla \times \vec{H} = \vec{J} + \frac{\partial \vec{D}}{\partial t} \tag{31}$$

$$\nabla \cdot \vec{D} = \rho_e \tag{32}$$

$$\nabla \cdot \vec{B} = 0 \tag{33}$$

$\vec{E}$: Electric field [V/m], $\vec{J}$: Electric current density [A/m²], $\vec{D}$: Displacement field [c/m²], $\vec{B}$: Magnetic flux density [T], $\vec{H}$: Magnetic field [A/m], they are then defined by (*Equations 34 to 36*).

$$\vec{D} = \varepsilon \cdot \vec{E} \tag{34}$$

$$\vec{H} = \frac{1}{\mu} \cdot \vec{B} \tag{35}$$

$$\vec{J} = \sigma \cdot \vec{E} \tag{36}$$

The boundary conditions of study area are demonstrated by the normal vectors (Equations 37-38)

$$n_x \cdot J_x + n_y \cdot J_y + n_z \cdot J_z = 0 \tag{37}$$

$$n_x \cdot A_x + n_y \cdot A_y + n_z \cdot A_z = 0 \tag{38}$$

The reference impedance equals to 50 Ω, the Lorentz force contribution equals to 10^9 N/m², the electrical conductivity in the coils is 3 10^7 S/m *figure 17a*, the surface current density in the coils is equal to 0.1 10^5 A/m *figure 17b*, the current density in the coils is equal to 1.5 10^{10} A/m² *figure 17c* and the electromagnetic volume loss density equals to 1.5 10^{13} W/m³ *figure 17d*.

FOREX Publication
Open Access | Rapid and quality publishing

International Journal of Electrical and Electronics Research (IJEER)
Research Article | Volume 11, Issue 4 | Pages 886-897 | e-ISSN: 2347-470X

<p style="text-align:center">(a)   (b)</p>
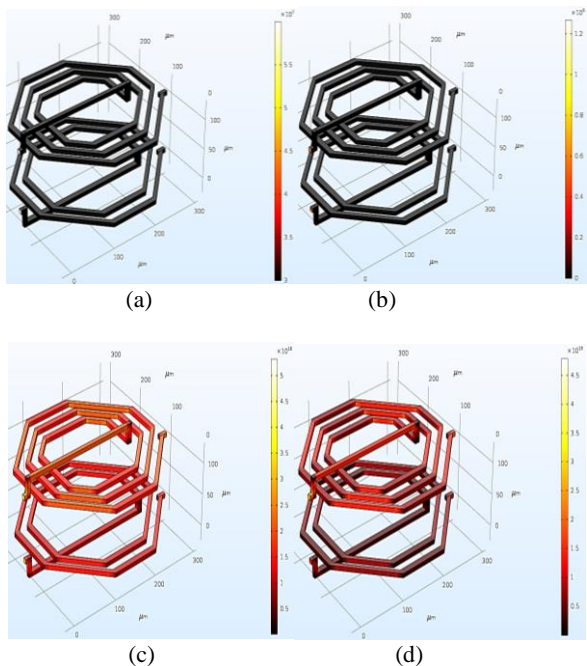

<p style="text-align:center">(c)   (d)</p>

Figure 17: (a) Electrical conductivity, (b) Surface current density, (c) Current density, (d) Electromagnetic volume loss density, in the spiral coils

7.2 Visualization of the Electromagnetic Behavior

Using Comsol Multiphysics 5.3 software and basing on finite elements method, we present the electromagnetic effects in the micro-transformer. For a good precision, we choose the extremely fine mesh.

<p style="text-align:center">(a)   (b)</p>
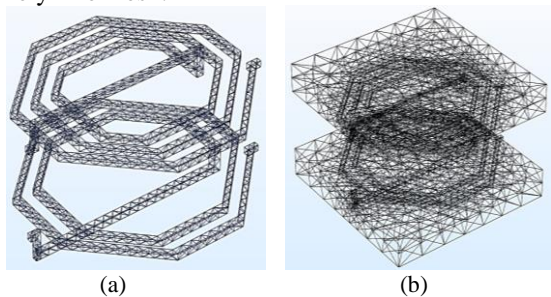
Figure 18: Mesh of the micro-transformer: (a) In air, (b) With different layers

Figure 18 shows the 3D extremely fine mesh of the integrated micro-transformer in the air and with all different layers
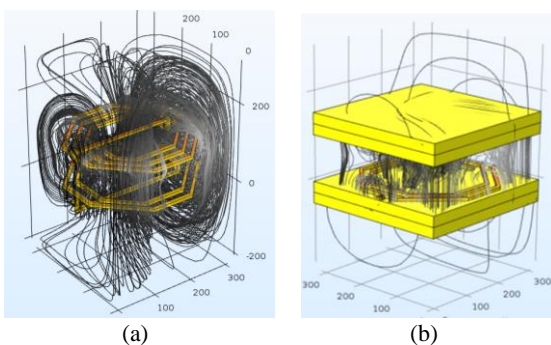

<p style="text-align:center">(a)   (b)</p>

Figure 19: Magnetic field lines in the micro-transformer: (a) In air, (b) With all layers

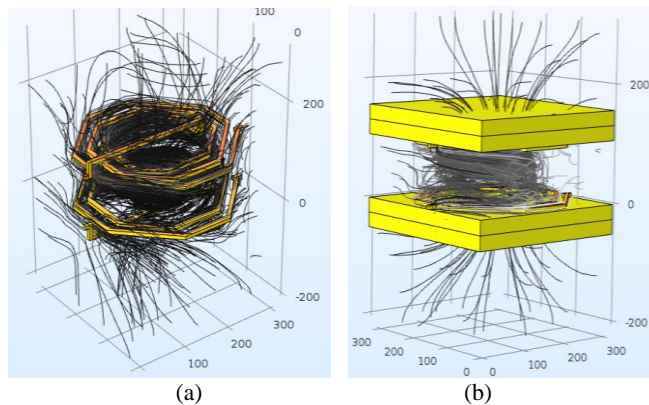<p style="text-align:center">(a)   (b)</p>

Figure 20: Power flow in the micro-transformer: (a) In air, (b) With all layers

Figure 19a shows the distribution of the magnetic field lines in the micro-transformer. We observe that there is an overflow of the magnetic field lines in all directions in the micro-transformer in the air and the lines occupy all the space limited by the simulator boundaries. Therefore, this distribution can make trouble of the nearby components in the circuit. In *figure 19b*, we observe that the overflow of the magnetic field lines is limited by the magnetic layer in NiFe ferrite thanks to its high permeability. Therefore, it restricts to disturb the nearby components in the same circuit.

In *figure 20*, we observe that the stack of the spiral planar coils on the ferrite layers allows to confine the power flow in the micro-transformer and avoids to lose the storage energy.
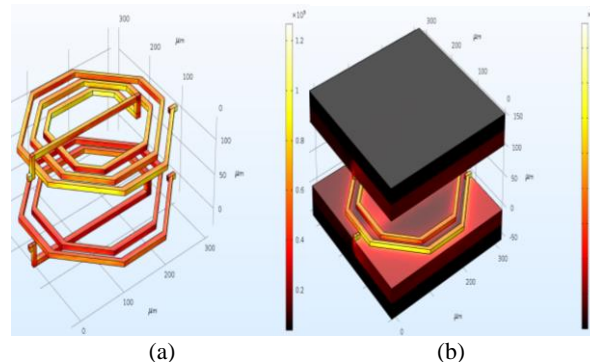

<p style="text-align:center">(a)   (b)</p>

Figure 21: Magnetic flux density in the micro-transformer: (a) In air, (b) With all layers

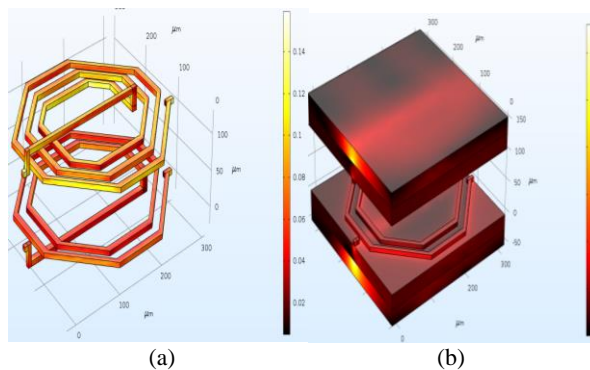<p style="text-align:center">(a)   (b)</p>

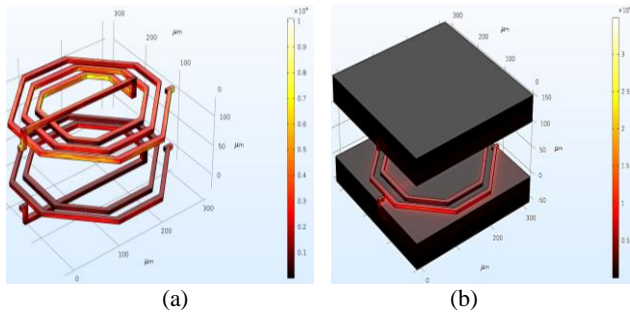**Figure 22:** Magnetic induction in the micro-transformer: (a) In air, (b) With all layers

Figure 23: Magnetic energy density in the micro-transformer: (a) In air, (b) With all layers
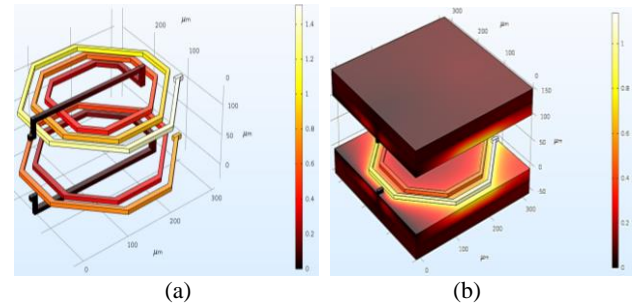

Figure 24: Magnetic field surface Maxwell stress tensor in the micro-transformer: (a) In air, (b) With all layers

Figure 25: Magnetic potential in the micro-transformer: (a) In air, (b) With all layers
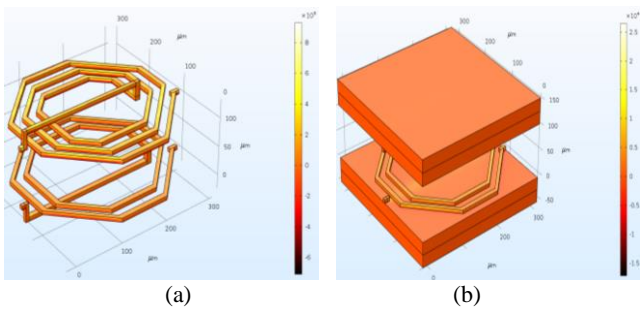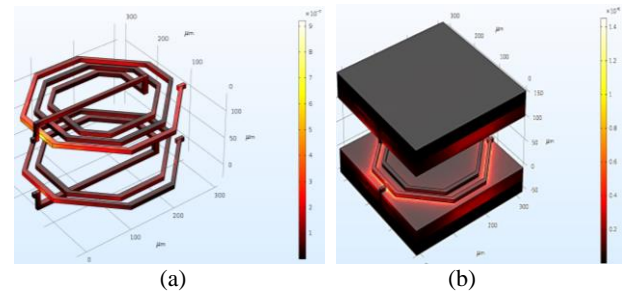
We observe that the magnetic flux density increases in the coils and achieves $1.5 \; 10^5$ A/m and spreads from the coils to the other stacked layers *figure 21*. The magnetic induction increases also and achieves 0.25 T in the entire micro-transformer *figure 22*. The magnetic energy density increases in the coils and achieves $1.2 \; 10^4$ J/m³ *figure 23*. The magnetic field surface Maxwell stress tensor increases and achieves $0.75 \; 10^4$ Pa in the coils *figure 24*. The magnetic potential increases in the entire micro-transformer and achieves $3 \; 10^{-5}$ Wb/m *figure 25*.

Figure 26: Electric field distribution in the micro-transformer: (a) In air, (b) With all layers

Figure 27: Electric potential in the micro-transformer: (a) In air, (b) With all layers

Figure 28: Electric displacement field in the micro-transformer: (a) In air, (b) With all layers
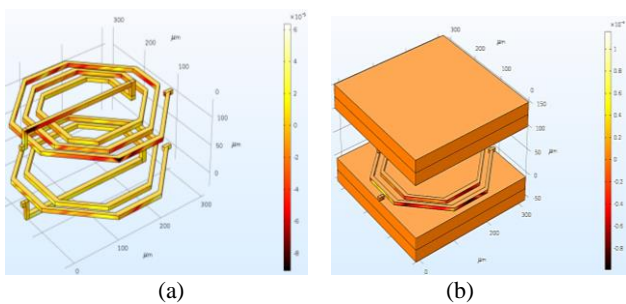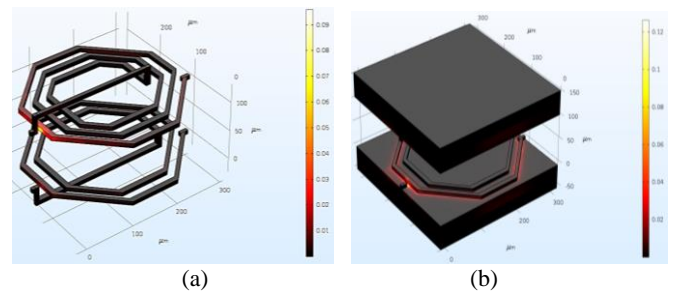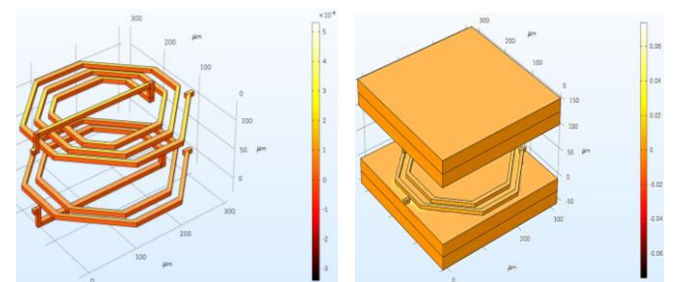

Figure 29: Electrical energy density in the micro-transformer: (a) In air, (b) With all layers

Figure 30: Electric field surface Maxwell stress tensor in the micro-transformer: (a) In air, (b) With all layers

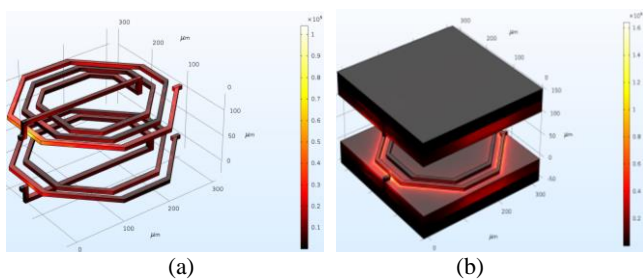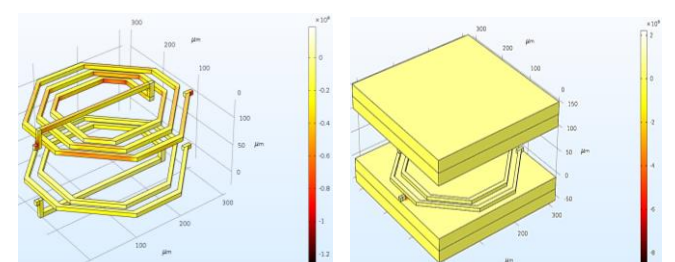**Figure 31:** Output power in the micro-transformer: (a) In air, (b) With all layers

We observe that the electric field increases in the coils and achieves 1.5 10⁵ V/m and spreads from the coils to the other stacked layers *figure 26*. The electric potential decreases for the micro-transformer with all layers to 1 V *figure 27*. The electric displacement field decreases in the coils 0.2 10⁻⁶ C/m² and spreads in the other layers *figure 28*. The electrical energy density increases to 0.025 J/m³ for the entire micro-transformer and achieves 0.12 in the input of the coils *figure 29*. The Electric field surface Maxwell stress tensor increases in the entire micro-transformer and achieves 0.02 Pa *figure 30*. The output power increases to 10⁹ W/m² for the entire micro-transformer *figure 31*.

8. MICRO-TRANSFORMER MODEL VALIDATION

In this section, we accomplish the simulation on DC-DC flyback micro-converter to check the integrated micro-transformer operation *figure 32*.
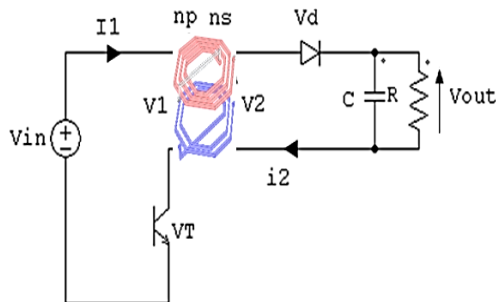

Figure 32: Flyback DC-DC micro-converter with the integrated micro-transformer
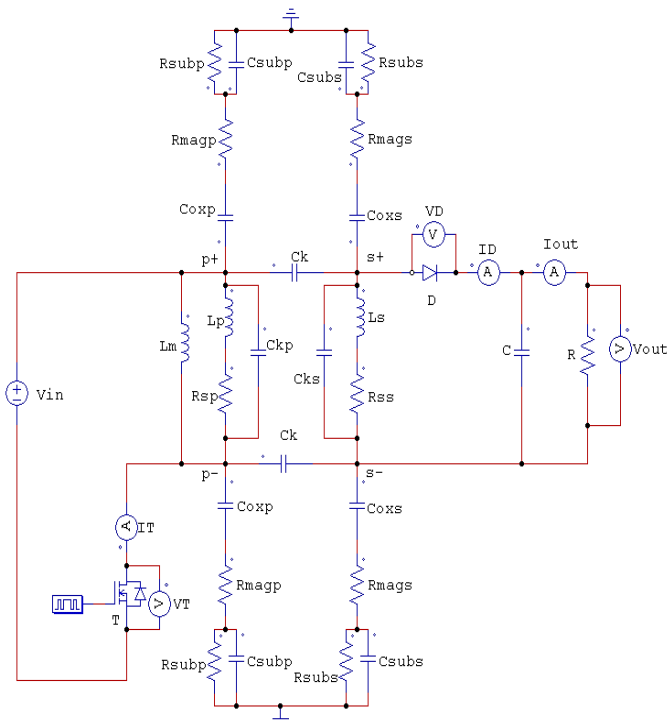

Figure 33: DC-DC flyback micro-converter with the integrated micro-transformer

Figure 33 shows the DC-DC flyback micro-converter containing the integrated micro-transformer equivalent electrical circuit. To accomplish the simulations, we need to calculate the load resistance R, load capacitance C and the magnetizing inductance Lm (Equations 39-41).

$$R = \frac{V_{out}}{i_{out}} \tag{39}$$

$$C = \frac{V_{in}}{32 \cdot L \cdot \Delta V_{out} \cdot f^2} \tag{40}$$

$$L_m = n_p^2 \cdot \frac{\mu_{MnZn} \cdot d_{out}^2}{2 \cdot e_{MnZn}} \tag{41}$$

After simulation on TINA software 9.0, the different curves are represented; the output voltage and current (Vout, Iout) *figure 34*, the transistor and diode voltages (VT, VD) and currents (IT, ID) *figure 35*, primary and secondary voltages (V1, V2) and currents (I1, I2) *figure 36*.
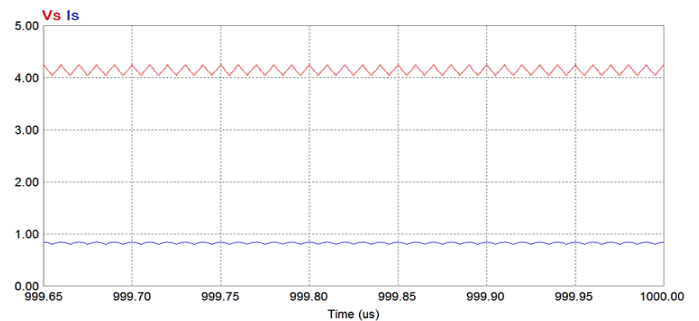

Figure 34: Output voltage and current of flyback micro-converter with the integrated micro-transformer
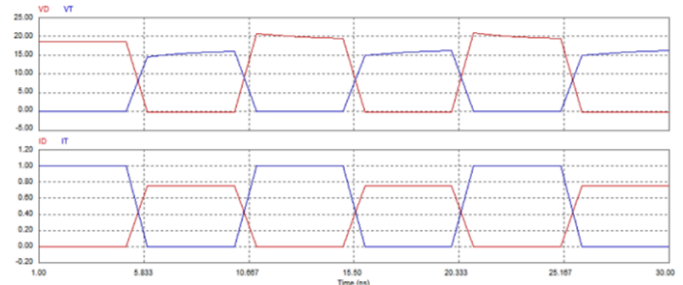

Figure 35: Voltage and current of both transistor and diode of flyback micro-converter with the integrated micro-transformer
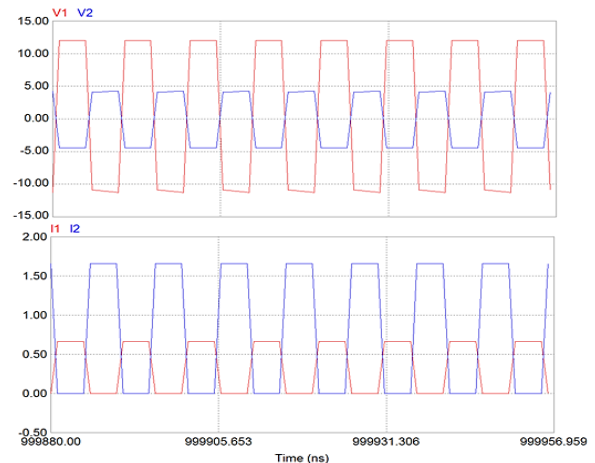

Figure 36: Voltage and current of both primary and secondary coils of integrated micro-transformer in flyback micro-converter

The obtained simulation results show that the output voltage Vout achieved is 4.25 V and the output current Iout is 0.85 A. The values are close to the main parameters (Vout = 5 V and Iout = 1A) of the DC-DC flyback micro-converter. This deline is due to the magnetic core losses in ferrite layers, the Joule losses in conductor coils, the capacitive losses between coils and also to the voltage drop across the transistor and diode. The primary coil V1 acheives 12 V and the secondary V2 is about 5 V. When the transistor is closed, the primary is directly connected to the input voltage source and the primary current increases storing energy in the magnetic layer of micro-transformer. When the transistor is opened, the diode become forward and the secondary allows the current to flow from the micro-transformer. The results confirm that micro-converter operates correctly and the dimensioning of the micro-transformer is well done.

8.1 Flyback Micro-Converter Efficiency

Efficiency η calculated by equation 42 represents the ratio of the output and input power of the micro-converter [14-18]. In *figure 37*, we notice that the output power 5 W of the DC-DC flyback micro-converter, containing the integrated micro-transformer, corresponds to an efficiency of 76.5%. Therefore, the micro-transformer dimensioning results are compatible with the integration in electronics and they are in accordance with the literature [19][26].

$$\eta = \frac{(V_{out} \cdot I_{out}) - (R_{seq} \cdot I_{out}^2) - (V_{in}^2/R_{seq})}{V_{out} \cdot I_{out}} \quad (42)$$
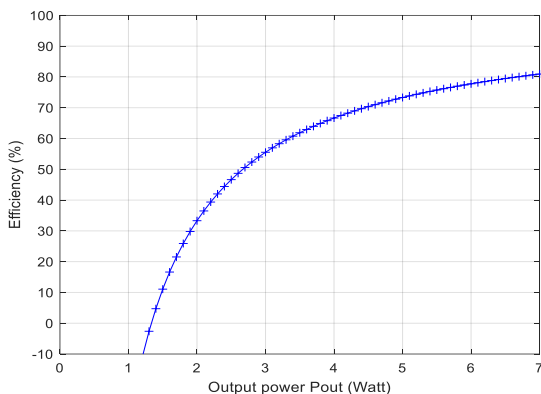

Figure 37: Flyback DC-DC micro-converter efficiency versus output power

8.2 Integration of the load capacitance

To fully integrate the flyback micro-converter, we can consider the micro-transformer coupling capacitance as the load capacitance of the micro-converter *figure 38*. The capacitor is located between metal spiral layers. It is considered as an integrated MIM (Metal-Insulator-Metal) capacitor. We compared between putting the dielectric material or the air between the coils of the micro-transformer. The capacitance is given by equation 43.

$$C_{gap} = \varepsilon_0 \cdot \varepsilon_r \cdot \frac{d_{out}^2}{t_{gap}} \quad (43)$$

The integration of the micro-transformer with the load capacitance of the micro-converter leads to create an integrated component called LCT (Inductor-Capacitance-Transformer). The inductor in this case is created from the leakage inductance [25-26].
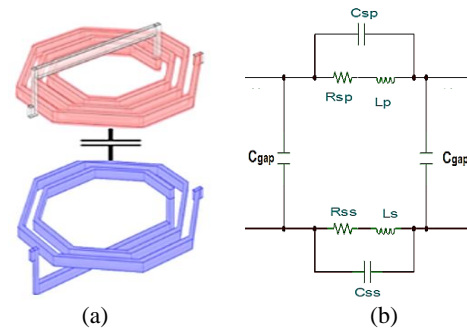

(a)   (b)

Figure 38: (a) Micro-transformer coupling capacitance as load capacitance of the micro-converter, (b) Equivalent circuit
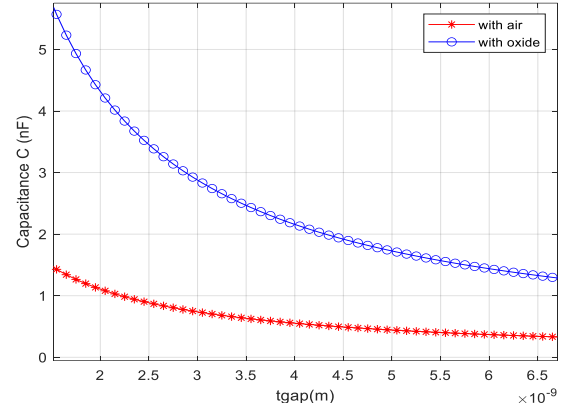
Figure 39: Capacitance between the coils of the micro-transformer versus gap thickness
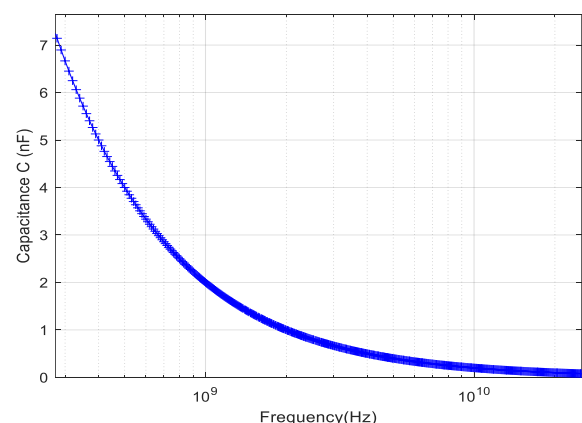
Figure 40: Capacitance between the coils of the micro-transformer versus frequency

Figure 39 shows the influence of the gap thickness t gap on the capacitance between the coils of the micro-transformer. We notice that adding the dielectric material allows to increase the capacitance, whereas the air permits to decrease it whatever the gap thickness. Besides, we notice from *figure 40* that the increase of the frequency permits to decrease the capacitance.

8.3 Low Pass Micro-Filter

The load capacitance C feeds the loads resistance R. these two passive components represent a micro-filter [27-28]. *Figure 41* shows the frequency response of the integrated micro-filter.
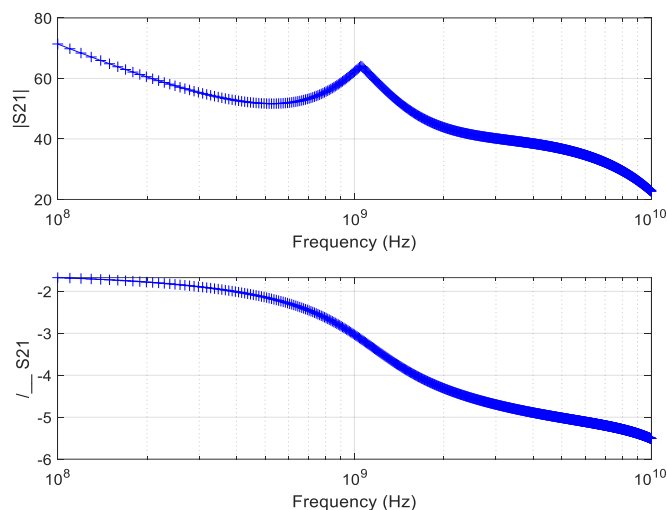

Figure 41: Attenuation and phase for low pass micro-filter

Figure 41 shows the Bode diagram of the attenuation ($|S21|$) and the phase ($/\_S21$) for the micro-filter versus frequency. We observe that the attenuation achieves 64 dB at the operating frequency 1 GHz. The phase mentions that the cut frequency is also at the operating frequency 1 GHz. Therefore, with the integration of the micro-capacitance, we have obtained a low pass micro-filter. It allows to pass the maximum low frequencies under 1 GHz.

9. CONCLUSION

This paper presents the design of a Flyback DC-DC micro-converter containing an integrated spiral planar octagonal micro-transformer. The first considered parameter was the shape of the coils. Octagonal spiral planar is the geometry of the stacked micro-transformer with three and two turns for primary and secondary coils respectively. This work is planned for the application requiring a conversion of energy of low power (5 W) and high frequency (1 GHz). We have fulfilled the geometric dimensioning using the Mohan's method, which is used for planar polygonal shapes and reduced number of turns. We have extracted the different electric parameters of the equivalent electrical circuit, which determines the parasitic effects created in stacked layers and generated at high frequency such as Joule effects losses in the coils, coupling capacitances and induced current in the magnetic substrate layers. The Q factor is an important characteristic for the coil's behavior, it presents the energy dissipation. Thinner coils and larger outer diameter allow to decrease the Q factor. Using finite element method, we have displayed the thermal and electromagnetic effects generated in the micro-transformer to confirm the advantage to use the magnetic core in ferrite. Hence, the insertion of ferrite with high permeability allows to confine the magnetic field lines, to limit the spread of the heat and decease the temperature value in order to avoid to disturb the close components in the integrated circuits. To validate our study, we have integrated the electrical circuit of the micro-transformer into a flyback micro-converter to test the good operation of the component. The results confirm that micro-converter operates correctly and the efficiency achieves 76.5%. Then, we have integrated the micro-capacitance to obtain a low pass micro-filter and we have concluded that the air is more comfortable than the dielectric materials. We conclude that the simulation results are in accordance with the literature and compatible with the integration in electronics.

Conflicts of Interest: "The authors declare no conflict of interest."

REFERENCES

[1] G. Lv et al., "A High-Efficiency Double-Side Silicon- Embedded Inductor for Integrated DC–DC Converter Applications," in IEEE Transactions on Electron Devices, vol. 68, no. 9, pp. 4801-4804, Sept. 2021, doi: 10.1109/TED.2021.3096923.

[2] Mayur V. Gojiya and Dr. Ketan P. Badgujar (2023), Effect of Test Cable Termination on Frequency Response of Transformer Winding. IJEER 11(1), 162-168. DOI: 10.37391/IJEER.110123.

[3] Anshuman Garg and Anjana Goen, (2014), Substrate Height and Dielectric Constant Dependent Performance of Rectangular Micro Strip Patch Antenna. IJEER 2(3), 36-39.

[4] X. Xing, N. X. Sun, and B. Chen, "High-Bandwidth Low-Insertion Loss Solenoid Transformers Using FeCoB Multilayers", IEEE Transaction on Power Electronics, vol. 28, no. 9, pp. 4395 – 4401, 2013.

[5] Hao Wu, Michael Lekas, Ryan Davies, Kenneth L. Shepard, Noah Sturcken, "Integrated Transformers with Magnetic Thin Films", IEEE Transaction on Magnetics, vol. 52, no. 7, pp. 8401204, 2016.

[6] Anshuman Garg and Anjana Goen, (2014), Enhancement Various Parameters of Rectangular Microstrip Patch Antenna with Metamaterial. IJEER 2(3), 28-31.

[7] Rajneesh kumar and Bimal Garg, (2014), Design of circular spiral antenna for mobile satellite Communication. IJEER 2(2), 16-20.

[8] E. S. Lee, J. H. Park, M. Y. Kim and S. H. Han, "An Integrated Transformer Design with a Center-Core Air-Gap for DAB Converters," in IEEE Access, vol. 9, pp. 121263-121278, 2021, doi: 10.1109/ACCESS.2021.3108837.

[9] M. Li, Z. Ouyang and M. A. E. Andersen, "Discovery of the Nearly Zero Flux Between Two Parallel Conductors in Planar Transformers," in IEEE Transactions on Power Electronics, vol. 37, no. 1, pp. 714-723, Jan. 2022, doi: 10.1109/TPEL.2021.3093171.

[10] Pankaj Agrawal and Nikhil Saxena, (2014), Leakage current analysis for stack based Nano CMOS Digital Circuits. IJEER 2(2), 5-11.

[11] L. Zheng, R. P. Kandula, K. Kandasamy and D. Divan, "New Modulation and Impact of Transformer Leakage Inductance on Current-Source Solid-State Transformer," in IEEE Transactions on Power Electronics, vol. 37, no. 1, pp. 562-576, Jan. 2022, doi: 10.1109/TPEL.2021.3101811.

[12] M. Lan et al., "An Improved Six-Port Equivalent-Circuit Model for Millimeter-Wave On-Chip Transformers With Accurate Coupling Factor Modeling," in IEEE Transactions on Microwave Theory and Techniques, vol. 69, no. 9, pp. 3989-4000, Sept. 2021, doi: 10.1109/TMTT.2021.3092342.

[13] K. Youssouf et al., "Design and Study of Interleaved and Face to Face Magnetic Microtransformers," in IEEE Transactions on Electron

Devices, vol. 61, no. 8, pp. 2873-2878, Aug. 2014, doi: 10.1109/TED.2014.2329334.

[14] S. Mohan, C.P.Yue, M. del Mar Hershenson, S. Wong, and T.H. Lee, "Modeling and characterization of on-chip transformers," International Electron Devices Meeting 1998, Technical Digest, IEEE, 1998, pp. 531-534.

[15] G. Lv et al., "A High-Efficiency Double-Side Silicon- Embedded Inductor for Integrated DC–DC Converter Applications," in IEEE Transactions on Electron Devices, vol. 68, no. 9, pp. 4801-4804, Sept. 2021, doi: 10.1109/TED.2021.3096923.

[16] D. Dinulovic, M. Shousha, M. Haug, S. Beringer and M. C. Wurz, "Comparative Study of Microfabricated Inductors/Transformers for High-Frequency Power Applications," in IEEE Transactions on Magnetics, vol. 53, no. 11, pp. 1-7, Nov. 2017, Art no. 4700107, doi: 10.1109/TMAG.2017.2734878.

[17] N. Zeidi, S. Kaziz, M. Hadj Said, L. Rufer, A. Cavallini, F. Tounsi, " Partial discharge detection with on-chip spiral inductor as a loop antenna", Review of Scientific Instruments 92, 094701 (2021)

[18] E. M. Dede et al., "Thermal Design, Optimization, and Packaging of Planar Magnetic Components," in IEEE Transactions on Components, Packaging and Manufacturing Technology, vol. 11, no. 9, pp. 1480-1488, Sept. 2021, doi: 10.1109/TCPMT.2021.3105003.

[19] L. Ying, H. Chunyue, Z. Xin, L. Tianming, G. Guangkuo, X. Guoji, T. Wenliang, "Influence of Compliant Layer Thickness on Stress and Strain of Solder Joints in Wafer Level Chip Scale Package under Thermal Cycle", IEEE 15th International Conference on Electronics Packaging Technology, 577-582, 2014.

[20] I. MS, MRK. Akanda, "3D Temperature Distribution of SiC MESFET Using Green's Function", Electrical and Computer Engineering, IEEE. 13-16, 2010

[21] Z. Ouyang and M. A. E. Andersen, "Overview of planar magnetic technology-fundamental properties", IEEE Trans. Power Electron., vol. 29, no. 9, pp. 4888-4900, Sep. 2014.

[22] M. K. Ranjram, I. Moon and D. J. Perreault, "Variable-inverter-rectifier-transformer: A hybrid electronic and magnetic structure enabling adjustable high step-down conversion ratios", Proc. 18th Workshop Control Model. Power Electron., pp. 1-8, Jul. 2017.

[23] H. K. Krishnamurthy et al., "A digitally controlled fully integrated voltage regulator with on-die solenoid inductor with planar magnetic core in 14-nm tri-gate CMOS", IEEE J. Solid-State Circuits, vol. 53, no. 1, pp. 8-19, Jan. 2018.

[24] S. A. Ansari, J. N. Davidson, M. P. Foster, and D. A. Stone, "Design and Analysis of a Fully-integrated Planar Transformer for LCLC Resonant Converters," in 2021 23rd European Conference on Power Electronics and Applications (EPE'21 ECCE Europe), 2021: IEEE, pp. P. 1-P. 8.

[25] B. Li, Q. Li, and F. C. Lee, "High-frequency PCB winding transformer with integrated inductors for a bi-directional resonant converter," IEEE Transactions on Power Electronics, vol. 34, no. 7, pp. 6123-6135, 2018.

[26] M. D'Antonio, S. Chakraborty, and A. Khaligh, "Planar Transformer with Asymmetric Integrated Leakage Inductance Using Horizontal Air Gap," IEEE Transactions on Power Electronics, 2021

[27] L. Pîslaru-Dănescu, A.M. Morega, G. Telipan, M. Morega, J.B. Dumitru, V. Marinescu, "Magnetic nanofluid applications in electrical engineering", IEEE Trans. on Magnetics, 49, 11, 2013.

[28] Yelda Veli, A.M. Morega, L. Pîslaru – Dănescu, M. Morega, „Numerical modeling of a flyback transformer with different magnetic media, for micro-power controllers", ICATE 2018, Craiova, Romania, Oct. 2018